continuum gamma-rays produced from higher energy thorium lines.

LP thorium counting rates correspond reasonably well with Apollo and Luna thorium soil sample measurements (*16*) for most of the abundance range (Fig. 7). However, there are some discrepancies between the LP GRS measurements and sample measurements as neither the Apollo 12 (open square), Apollo 15 (closed diamond) or Apollo 14 (closed circle) data fall uniquely on a straight line with the remaining data. It is probable that the discrepancies result because the Apollo sample measurements simply do not provide an accurate measure of composition for the 150-km-radius footpoint seen by the LP GRS. However, even if Th is locally enhanced (at the Apollo 14 site, for example), the GRS measurements average out these enhancements over ~150 km. As shown in Fig. 7, the maximum thorium counting rate (located approximately 500 km from the Apollo 14 landing site) is only 3% greater than the Apollo 14 counting rate. Thus any localized thorium enhancements, if they exist, have been averaged out.

Counting rate map for 7.6-MeV gamma-rays. The statistics for the counting rate of the 7.6-MeV gamma-rays dominated by iron are not as high as for thorium and potassium. Furthermore, overlap from a 7.72-MeV aluminum line cannot yet be separated from the 7.6-MeV iron lines. Nevertheless, the available data (Figs. 1 and 8) show that the counts around 7.6 MeV vary substantially between the lunar maria and highlands regions.

The global distribution of iron inferred from the GRS data (Fig. 8) is comparable to that obtained by both the LP thermal and fast neutron detector (*17*) and earlier Clementine data (*18*). For example, high iron abundances are seen in the nearside mare, the SPA, and Mare Australe. However, we also see high gamma-ray counting rates in regions that do not appear to correlate with the high iron regions from the Clementine data, for example, east of Mare Serenitatis and Mare Frigoris. Although the LP neutron data also suggest there are high iron abundances in these regions, there are some regions of high gamma-ray counting rates on the lunar farside (for example, 90°W to 165°W and 45°N to 85°N) that do not correlate with high iron regions in either the neutron data or the Clementine data. Most of these regions are lunar highlands thought to have relatively high aluminum abundance and relatively low iron abundance. Because the 7.72-MeV aluminum gamma-ray line is the most intense of the few gamma-ray lines that can produce an interference with the 7.6-MeV iron lines (*8*), these data suggest that some of the anomalous high count rate regions may be due to elevated aluminum abundances.

References and Notes

1. The NASA Lunar Exploration Science Working Group (LExSWG), *A Planetary Science Strategy for the Moon*, JSC-25920 (1992).
2. S. R. Taylor and T. M. Esat, *Earth Processes: Reading the Isotopic Code* (*Geophys. Monogr. 95*, American Geophysical Union, Washington, DC, 1996), pp. 33–46.
3. P. H. Schultz and P. D. Spudis, *Proc. Lunar Planet. Sci. Conf.* **10**, 2899 (1979); *Nature*, **302**, 233, (1983).
4. A. E. Metzger, in *Remote Geochemical Analysis: Elemental and Mineralogical Composition*, C. M. Pieters and P. A. J. Englert, Eds. (Cambridge Univ. Press, Cambridge, 1993), pp. 341–363.
5. W. C. Feldman *et al.*, *Proc. Lunar Planet. Sci. Conf.* **27**, 355 (1996); W. C. Feldman *et al.*, *Nucl. Instrum. Methods Phys. Res. A*, in press.
6. Events triggering only by the bismuth germanate (BGO) crystal of the GRS are accepted gamma-ray events; events triggering both by the BGO and anticoincidence shield (ACS) are rejected and are due to energetic charged particles and gamma-rays that deposit a fraction of their energy in the ACS (*5*).
7. The LP GRS has an energy (E) resolution of 10.5% at 0.662 MeV and scales as $E^{-1/2}$ (*5*).
8. R. C. Reedy, *Proc. Lunar Planet. Sci. Conf.* **9**, 2961 (1978).
9. P. R. Truscott *et al.*, *IEEE Trans. Nucl. Sci.* **42**, No. 4, 946, (1995); P. R. Truscott, *ibid.* **43**, No. 3, 1510 (1996).
10. L. Haskin and P. Warren, in *Lunar Sourcebook, A User's Guide to the Moon*, G. H. Heiken, D. T. Vaniman, B. M. French, Eds. (Cambridge Univ. Press, Cambridge, 1991), pp. 357–474.
11. D. E. Smith, M. T. Zuber, G. A. Neumann, F. G. Lemoine, *J. Geophys. Res.* **102**, 1591 (1997); P. G. Lucey, P. D. Spudis, M. Zuber, D. Smith, E. Malaret, *Science* **266**, 1855 (1995).
12. The channel to energy calibration of the GRS is 0.018 MeV per channel. The energy bands being summed therefore consist of 22 channels for thorium and 11 channels for potassium.
13. F. Hörz, R. Grieve, G. Heiken, P. Spudis, A. Binder, in (*10*), pp. 61–120.
14. L. A. Haskin, *J. Geophys. Res.* **103**, 1679 (1998).
15. B. Ray Hawke and J. W. Head, *Proc. Lunar Planet. Sci. Conf.* **9**, 3285 (1978); P. D. Spudis, *ibid*, p. 3379.
16. R. L. Korotev, *J. Geophys. Res.* **103**, 1691 (1998).
17. W. C. Feldman *et al.*, *Science* **28**, 1489 (1998); R. C. Elphic *et al.*, *ibid.*, p. 1493.
18. P. G. Lucey, D. T. Blewett, B. R. Hawke, *J. Geophys. Res.* **103**, 3679 (1998).

19. We thank R. C. Reedy for helpful comments regarding this manuscript and we thank P. D. Spudis and another referee for their detailed comments. This work was supported in part by Lockheed-Martin and conducted under the auspices of the U.S. Department of Energy.

13 July 1998; accepted 11 August 1998

Major Compositional Units of the Moon: Lunar Prospector Thermal and Fast Neutrons

W. C. Feldman,* B. L. Barraclough, S. Maurice, R. C. Elphic, D. J. Lawrence, D. R. Thomsen, A. B. Binder

Global maps of thermal and fast neutron fluxes from the moon suggest three end-member compositional units. A high thermal and low fast neutron flux unit correlates with the lunar highlands and is consistent with feldspathic rocks. The South Pole–Aitken basin and a strip that surrounds the nearside maria have intermediate thermal and fast neutron flux levels, consistent with more mafic rocks. There appears to be a smooth transition between the most mafic and feldspathic compositions, which correspond to low and high surface altitudes, respectively. The maria show low thermal and high fast neutron fluxes, consistent with basaltic rocks.

Neutrons are generated by interactions between galactic cosmic rays and surface material in all planetary bodies that have sufficiently thin atmospheres. Subsequent interactions of the neutrons with surrounding material produce a steady-state, equilibrium energy spectrum that spans from the fast neutron range, where neutrons are born (energies, E, greater than several hundred thousand electron volts), to the thermal energy range ($E < 0.3$ eV), where neutrons are absorbed. Neutron energy spectra are therefore expected to reflect the composition of near-surface planetary layers. Simulations of equilibrium spectra indicate that the fast neutrons provide information primarily about the Fe and Ti content of soils (*1–3*). Epithermal neutrons (energies between ~0.3 eV and several hundred thousand electron volts) reflect primarily the abundance of hydrogen (*4*), and thermal neutrons reflect the abundance of neutron-absorbing nuclei, primarily Fe, Ti, K, Gd, and Sm (*4–7*).

The Lunar Prospector (LP) neutron spectrometer (NS) measures the flux of thermal, epithermal, and fast neutrons. Thermal and epithermal neutrons are measured using two ^{3}He-filled gas proportional counters and associated electronics (*8*). One of the counters is covered with a 0.63-mm-thick sheet of Cd, which, because of its high (>10,000 barns)

W. C. Feldman, B. L. Barraclough, R. C. Elphic, D. J. Lawrence, D. R. Thomsen, Los Alamos National Laboratory, MS D-466, Los Alamos NM 87545, USA. S. Maurice, Observatoire Midi-Pyrenees, 14 avenue Ed Belin, 31400 Toulouse, France. A. B. Binder, Lunar Research Institute, 1180 Sunrise Drive, Gilroy, CA 95020, USA.

*To whom correspondence should be addressed. E-mail: wfeldman@lanl.gov

absorption cross section, shields the counter from neutrons with energies less than ~0.3 eV. The second counter is covered with an identical thickness of Sn (to ensure a similar response to background fluxes) and responds to neutrons having energies up to ~1000 eV.

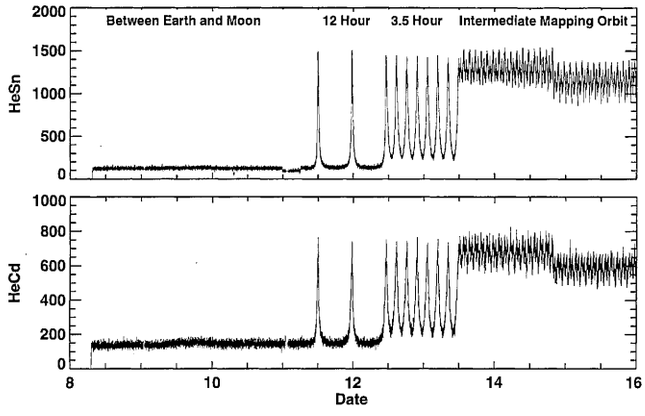

Fig. 1. Counts registered by the tin-wrapped (HeSn) and cadmium-wrapped (HeCd) NS sensors during successive 32-s integration periods from instrument turn-on (8 January 1998) to 16 January 1998. LP was launched on 6 January 1998, the NS was operational by 8 January, and lunar orbit insertion occurred on 11 January. Backgrounds were recorded by each counter operated at its low energy threshold during the first 3.5 days of operation when the spacecraft was far from both Earth and moon. The reality of this background was verified by lowering the high voltage on the HeSn detector for a short time on 11 January. The time sequence of HeSn counting rates responded with a step function decrease that was not recorded by the HeCd detector. Counter thresholds were commanded to their operational values late on 14 January, as seen by the sharp decrease in counting rates in both counters.

Because the two counters are matched, the difference in their counting rates yields a measure of the thermal neutron flux ($E < 0.3$ eV). Fast neutrons are measured using the anticoincidence shield (ACS) of the LP gamma-ray spectrometer (*8*).

Neutron flux backgrounds in space are low because free neutrons are unstable, with a mean life to beta decay of ~900 s. To be detected by LP, neutrons must therefore be produced locally. All of the science instruments on the LP were placed at the ends of 2.5-m booms to minimize spacecraft neutron flux backgrounds (*9*). This separation and the spacecraft's low mass were sufficient to reduce backgrounds to acceptable levels (measured during transit between Earth and moon; Fig. 1). The first two orbits of LP around the moon had a 12-hour period, followed by seven 3.5-hour-period orbits, then by many intermediate mapping orbits (~90 km periselene and 150 km aposelene), until 16 January 1998, when LP was placed into its final mapping orbit at an altitude of 100 ± 20 km (Fig. 1). Residual variations in detector

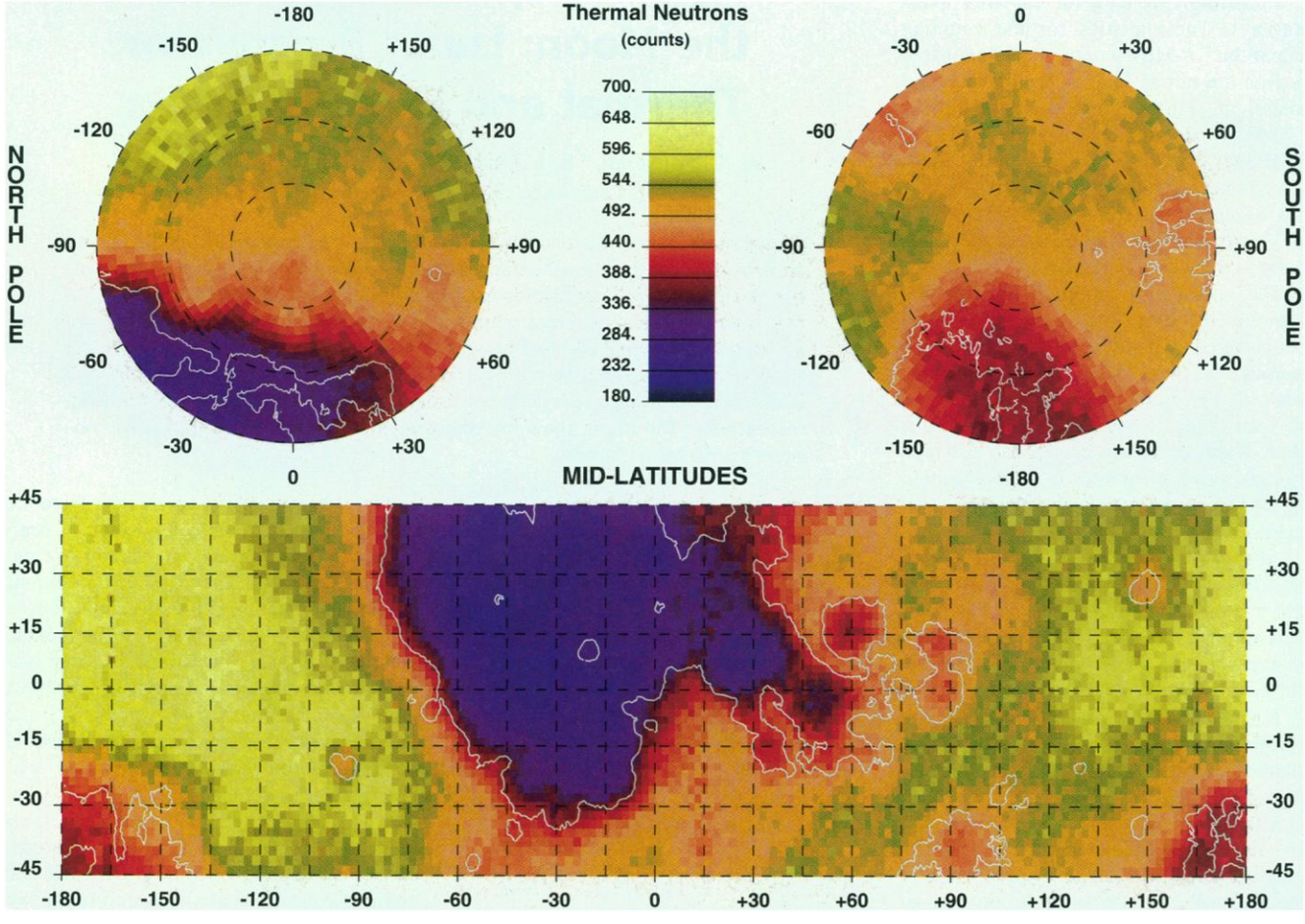

Fig. 2. Global map of the thermal neutron counting rate (given by counts per 32-s spectral integration period). Data acquired during mapping cycles 1 through 12 (16 January to 27 June 1998) are combined and have been partially corrected for instrument response function and variations in the flux of galactic cosmic rays. A basemap constructed using Clementine albedo data (*19*), showing various lunar features, overlays the thermal neutron counting rates.

counting rates after midday on 13 January reflect, for the most part, compositional variations of the lunar surface. Here, we report on neutron fluxes measured between 16 January and 27 June 1998.

Thermal and fast neutron maps. The difference in counts registered by the Sn- and Cd-covered counters in successive 32-s counting intervals was binned into equal area pixels, equivalent to 2° by 2° latitude-longitude bins at the equator. These data were segregated into individual 2-week map cycles that each correspond to complete coverage of the moon. Adjacent odd and even cycles were first registered for overlapping data and then added together to compensate for day-night and hot-cold differences that result from the combined effects of lunar gravity and Doppler effects. Lunar gravity reduces the energy of escaping thermal neutrons as they travel from the lunar surface to the spacecraft, and it bends neutrons away from the zenith because their orbits are elliptical or hyperbolic (*10*). Accounting for the Doppler effect is important because LP orbits the moon at a speed (1.64 km s^{-1}) that is comparable to the speed of a thermal neutron (2.2 km s^{-1} at a temperature of 293 K) (*11*). Accepted counts were then corrected for the nonspherical response function of the NS and for variations in the flux of galactic cosmic rays.

The global map of thermal neutron counting rates (Fig. 2) reveals several areas of high and low intensity. The lowest intensity overlaps the maria that fill the large nearside basins, as seen in visible reflectance maps of the moon. These low intensities reflect, for the most part, the combined large absorption cross sections of Fe, Ti, K, Gd, and Sm and their relatively large concentration in mare basalt (*5–7*).

A well-defined intermediate intensity generally fills the South Pole–Aitken (SPA) basin (56°S, 180°W). It is similar to that registered from Crisium (18°N, 59°E), Smythii (2°S, 87°E), Marginis (20°N, 84°E), Australe (52°S, 95°E), and a rim that surrounds all of the nearside basins. Although some of these rates may reflect the relatively poor spatial resolution of the LP thermal neutron sensor (footprint diameter ~450 km), which cannot fully resolve small-scale features such as Orientale and Moscoviense, this reason does not necessarily apply to SPA or Australe. Instead, the intermediate counting rates there reflect the presence of rocks that are distinct from those in surrounding areas and, perhaps, the mixing of basaltic and highlands material in soils at a scale size (<100 km) that is not resolved by the NS.

A roughly annular region of high thermal neutron intensities appears to ring the SPA basin. This region corresponds to the highlands, as shown by the topography measured using the Clementine laser altimeter (*12*) and modeled from gravity maps (*13*). This annulus is broken by local regions of low intensity that mark individual impact craters or basins. Specific examples are Orientale (20°S, 95°W), Moscoviense (25°N, 150°E), Australe (52°S, 95°E), Humorum (24°S, 40°W), and Nubium (21°S, 15°W).

The three general regions are delineated in peaks in the histogram of thermal neutron intensities at about 290, 400, and 520 counts

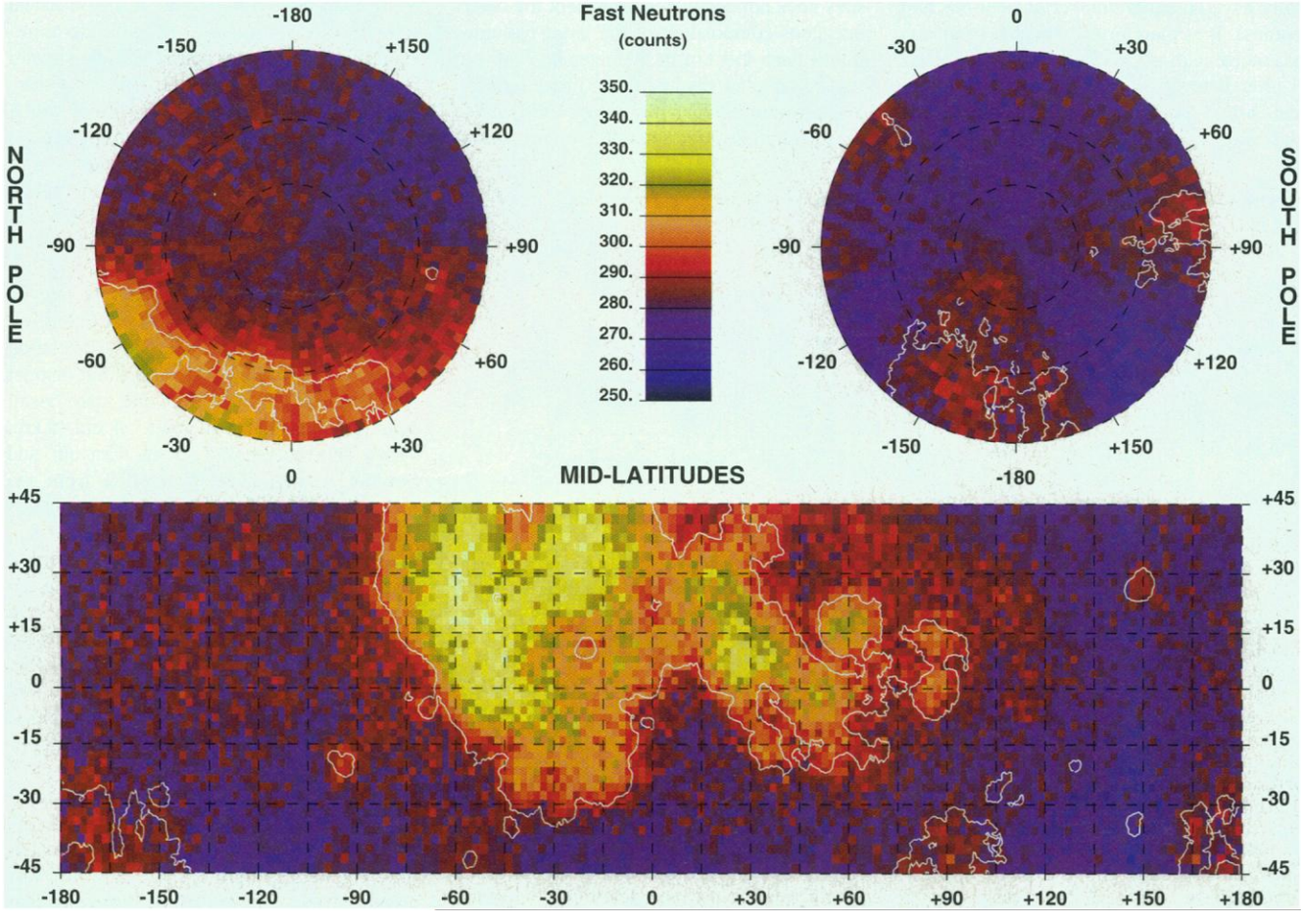

Fig. 3. Global map of the fast neutron counting rate (given by counts per 32-s spectral integration period). Data acquired during mapping cycles 1 through 12 (16 January to 27 June 1998) are combined and have been partially corrected for instrument response function and variations in the flux of galactic cosmic rays. A basemap constructed using Clementine albedo data (*19*), showing various lunar features, overlays the fast neutron counting rates.

per 32-s spectrum (*14*). They probably correspond to three broadly different surface composition units. We infer that these units correspond to a wide range of mare basalts, mafic highland rocks, and feldspathic highland rocks, respectively.

A map of integrated fast neutron counts is shown in Fig. 3. These counts weight the low-energy portion of the fast neutron flux spectrum most heavily because the efficiency of the ACS to neutrons decreases as E^{-1} (*15*). Enhanced counting rates mark the locations of the various basin-filled maria on the nearside of the moon, and weaker enhancements mark the SPA, Australe, Orientale, Marginis, Smythii, Humboldtianum, and Moscoviense formations. This pattern matches the regions of high Fe and Ti abundances inferred from spectral reflectance measurements made by Clementine (*16*), and those of low thermal neutron flux (Fig. 2) [see also (*7*)]. Enhanced fast neutron emission from Fe and Ti probably reflects the higher number of neutrons relative to protons within Fe and Ti nuclei (each containing an excess of four neutrons) than found in lower mass nuclei (which typically have an equal number of neutrons and protons). It is therefore reasonable to expect that more neutrons will escape from Fe and Ti after being hit by a galactic cosmic ray than would emerge from O or Si, a fact confirmed by simulations (*1, 2*).

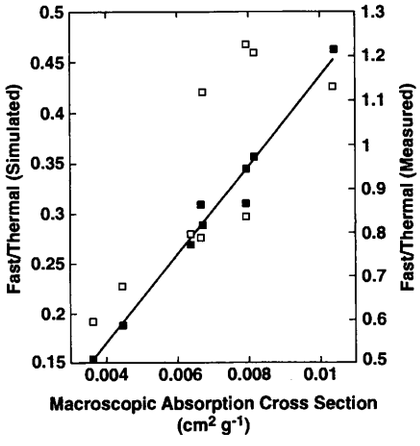

Fig. 4. Correlation of the simulated (filled-square symbols) and measured (open-square symbols) fast/thermal neutron counting rates (both arbitrary units) as a function of the calculated macroscopic neutron absorption cross section. In order of increasing cross section, the points correspond to Apollo 16, Luna 20, Apollo 17, Luna 24, Apollo 15, Luna 16, Apollo 14, Apollo 12, and Apollo 11. Bulk compositions of the soils and regolith breccias from the six Apollo landing sites and the three Luna returned-sample sites (*17*) have been used to calculate the effective absorption cross sections for each site. The line gives the linear regression between simulated counts and the macroscopic absorption cross section (r = 0.99).

Correlation with composition of returned samples. Translation of thermal counting rates to surface composition requires intercalibration with surface samples of known composition. This information is available from measurements of the composition of soils and regolith breccias returned to Earth by the Apollo and Luna missions (*17*). The correlation between the measured ratio of fast-to-thermal neutron intensities and the macroscopic absorption cross sections from the samples (Fig. 4) is fair, with a correlation coefficient r = 0.71. The measured correlation can be improved slightly by repositioning the Apollo and Luna subsatellite footpoints within the spatial resolution elements of the neutron sensor, yielding r = 0.78. In contrast, the correlation is better between the fast-to-thermal neutron flux ratios simulated using ONEDANT (*18*) and the macroscopic absorption cross section, also shown in Fig. 4 (r = 0.99).

These results imply either that measured thermal neutron intensities are not uniquely related to composition, or that the composition of soils returned from discrete landing sites does not adequately represent the heterogeneous composition of the larger volumes (more than 450 km in diameter by ~50 cm deep) sampled by neutron measurements made from orbit at an altitude of 100 km. We believe the last interpretation is more consistent with the data. Otherwise it would be difficult to explain the good correlation obtained between measured thermal-to-fast neutron flux intensities and the Fe and Ti abundances inferred from Clementine spectral reflectance data (*7*).

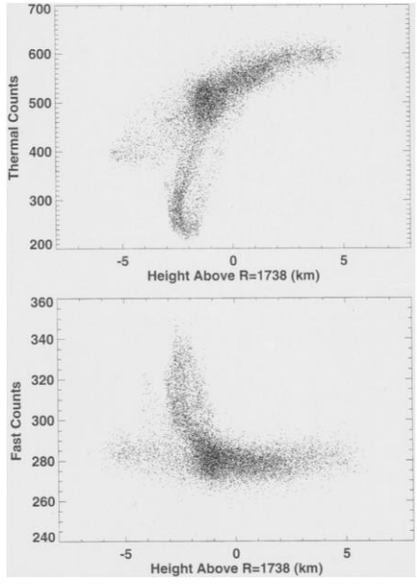

Fig. 5. Correlation between measured thermal neutron (top) and fast neutron (bottom) counting rates (given by counts per 32-s spectral integration period), and the height of the lunar surface above the mean datum measured by Clementine. Clementine-determined altitudes were smoothed to 14.5° spatial resolution to match the footprint size resolution of the thermal neutrons in the upper plot, and to 5.5° resolution to match that of the fast neutrons in the lower plot.

Correlation with albedo and topography. The thermal and fast neutron intensities (Figs. 2 and 3) resemble the visible albedo map of the moon measured by Clementine (*19*) (r = 0.80 and r = −0.76 for thermal and fast neutrons, respectively). The principal cause of lunar albedo variations is the presence or absence of Fe-rich mare basalts. The correlation of thermal counts with the albedo is improved by eliminating terrain covered by KREEP (potassium, rare-earth elements, and phosphorus) basalt (*7*). The correlation in the area bounded by ±30° latitude and 20° to 180°E is 0.91.

The overall correlation between thermal and fast neutron counting rates and surface topography is not as good. However, scatter plots of thermal and fast neutron counts as a function of smoothed height above 1738 km (Fig. 5) are revealing. Three major spurs are evident in both plots. The nearly vertical spurs between −4 and −5 km altitude correspond to the nearside maria. The downward (upward) sloping spur to the left in the thermal (fast) correlation corresponds to the SPA basin. It connects smoothly to the spur on the right that corresponds to the highlands. The last two spurs appear to be a single entity that extends from a mafic compositional unit that marks the SPA (intermediate abundance of Fe and Ti) to a feldspathic compositional unit that marks the highlands (relatively low Fe and Ti abundances). Also apparent in the fast neutron-to-topographic altitude correlation (at the bottom of Fig. 5) is a weak but distinct spur between the main SPA and mare basalt spurs at heights between about −4 and −5 km. These data correspond to the Crisium and Smythii basins. Their distinction from the main vertical spur must reflect a distinct basaltic composition.

Summary and discussion. Thermal neutron flux intensities measured using the NS cover a substantial dynamic range (about a factor of 3.5 for thermal neutrons and a factor of 1.25 for fast neutrons) that correlates reasonably well with visible and topographic features on the moon. Three end-member compositional units are delineated. The first, consisting of generally low thermal and high fast intensities, corresponds to the maria deposits that fill the large nearside basins. The second, consisting of generally high thermal and low fast counting rates, delineates the highlands that form a rough annulus centered on SPA. The third unit, characterized by intermediate thermal and fast intensities, is associated with SPA, Humboldtianum, and a rim that

surrounds the nearside basins. These last deposits may reflect a separate rock type that is mafic in composition, or may merely reflect numerous, unresolved small-area basalt deposits that dot these regions.

The overall correlation is sufficient to suggest that the measured thermal and fast neutron fluxes, on spatial scales on the order of 200 km (fast neutrons) to 450 km (thermal neutrons) diameter areas (for an LP altitude of 100 km), reveal a smooth transition from a predominantly mafic composition at low altitudes to a predominantly feldspathic composition at high altitudes. The more mafic deposits result from excavation of highlands material by the impacts that created all of the big basins such as SPA, thereby exposing material from the lower crust and perhaps the upper mantle (*13*), whereas the feldspathic composition reflects the top of the crust that is exposed in the highlands.

References and Notes

1. D. M. Drake, W. C. Feldman, B. M. Jakosky, *J. Geophys. Res.* **93**, 6353 (1988).
2. J. Masarik and R. C. Reedy, *ibid.* **101**, 18891 (1996).
3. R. C. Reedy *et al.*, *Meteor. Planet. Sci.* **33** (no. 4, suppl.), A127.
4. W. C. Feldman *et al.*, *J. Geophys. Res.* **102**, 25565 (1997).
5. R. E. Lingenfelter, E. H. Canfield, V. E. Hampel, *Earth Planet. Sci. Lett.* **16**, 355 (1972).
6. W. C. Feldman, R. C. Reedy, D. S. McKay, *Geophys. Res. Lett.* **18**, 2157 (1991).
7. R. C. Elphic *et al.*, *Science* **281**, 1493 (1998).
8. W. C. Feldman *et al.*, *Nucl. Instrum. Methods Phys. Res. A*, in press.
9. A. B. Binder, *Science* **281**, 1475 (1998).
10. W. C. Feldman, D. M. Drake, R. D. O'Dell, F. W. Brinkley Jr., R. C. Anderson, *J. Geophys. Res.* **94**, 513 (1989).
11. W. C. Feldman and D. M. Drake, *Nucl. Instrum. Methods Phys. Res.* **A245**, 182 (1986).
12. D. E. Smith, M. T. Zuber, G. A. Neumann, F. G. Lemoine, *J. Geophys. Res.* **102**, 1591 (1997).
13. M. A. Wieczorek and R. J. Phillips, *ibid.* **103**, 1715 (1998).
14. W. C. Feldman *et al.*, *Science* **281**, 1496 (1998).
15. R. C. Byrd and W. T. Urban, *LANL Doc. LA-12833-MS* (1994).
16. P. G. Lucey, D. T. Blewett, B. R. Hawke, *J. Geophys. Res.* **103**, 3679 (1998).
17. L. Haskin and P. Warren, in *Lunar Sourcebook, a User's Guide to the Moon*, G. H. Heiken, D. T. Vaniman, B. M. French, Eds. (Cambridge Univ. Press, Cambridge, 1991), pp. 357–474.
18. R. E. Alcouffe *et al.*, *LANL Manual LA-7369-M*, rev. 2 (1995).
19. P. G. Lucey, P. D. Spudis, M. Zuber, D. Smith, E. Malaret, *Science* **266**, 1855 (1994).

20. Supported in part by Lockheed Martin under contract to NASA and conducted under the auspices of the U.S. Department of Energy.

13 July 1998; accepted 10 August 1998

Lunar Fe and Ti Abundances: Comparison of Lunar Prospector and Clementine Data

R. C. Elphic,* D. J. Lawrence, W. C. Feldman, B. L. Barraclough, S. Maurice, A. B. Binder, P. G. Lucey

The Lunar Prospector neutron spectrometer data correlate well with iron and titanium abundances obtained through analysis of Clementine spectral reflectance data. With the iron and titanium dependence removed, the neutron spectrometer data also reveal regions with enhanced amounts of gadolinium and samarium, incompatible rare earth elements that are enriched in the final phases of magma crystallization. These regions are found mainly around the ramparts of the Imbrium impact basin but not around the other basins, including the much larger and deeper South Pole–Aitken basin. This result confirms the compositional uniqueness of the surface and interior of the Imbrium region.

The surface of the moon provides a record of the early evolution of the Earth-moon system through the period of heavy bombardment ~4 billion years ago. In contrast, most terrestrial rocks are much younger. Throughout the moon's history large impacts have excavated material from the lower crust (and possibly the mafic upper mantle) and deposited it on the surface. Basaltic volcanism during and after the heavy bombardment epoch flooded some impact basins with material derived from partial melting of the upper mantle and lower crust. Study of these materials thus provides a window into the moon's interior. Whereas most of our understanding of lunar composition is derived primarily from returned Apollo and Luna samples, the question remains to what extent these samples are representative of the whole moon.

A major step toward a global assessment of lunar surface chemistry was provided by analysis of spectral reflectance data returned by the Clementine mission. Comparison of the spectral reflectance properties and chemical compositions of lunar soils returned by the Apollo and Luna missions, and remote measurement of the spectral properties of the Apollo and Luna sample collection sites by Clementine, led to the development of algorithms that derive the abundance of FeO and TiO_2 from spectral properties of lunar soils and surface units with 1 to 2 weight % accuracy. By applying these algorithms to Clementine global imaging, it has been possible to infer the quantitative abundance of FeO and TiO_2 within $\pm 80°$ latitude (*1–4*) at resolutions approaching 100 m. The approach was calibrated with lunar samples returned from a relatively small area of the lunar nearside, and it is possible that areas distant from the landing sites, such as the farside, might have different mineralogies. Thus, the inferred FeO and TiO_2 values might be spurious there (*5*). Here, we test the validity of the Clementine spectral reflectance (CSR) method with independent analyses of Fe and Ti, using data from the Lunar Prospector (LP) neutron spectrometer (*6, 7*).

The neutron spectrometer measures neutrons at thermal (0.001 to 0.3 eV), epithermal (0.3 eV to 500 keV), and fast (500 keV to 8 MeV) energies. Lunar neutrons are created by the interaction of galactic cosmic rays with the nuclei in the lunar regolith; they are produced in the fast regime at high energies as a direct result of spallation. These neutrons inelastically scatter off of other nuclei in the soil, losing energy as they pass through the epithermal regime. When their energies approach that corresponding to the temperature of the ambient regolith (thermal regime), the neutrons are captured by nuclei that have large cross sections for thermal neutron absorption (*8*). Iron and titanium are the most abundant elements with large absorption cross sections; consequently, they have considerable influence on thermal neutron fluxes. In addition, Fe and Ti evidently produce more fast neutrons than elements with lower atomic numbers (*9*). Consequently, when LP is above the Fe- and Ti-rich maria, the neutron spectrometer detects a higher fast neutron flux and a lower thermal neutron flux (*6, 7*). We report on neutron data acquired during the first 6 months of the LP mapping mission, beginning 16 January 1998.

The neutron spectrometer measures the net production of fast neutrons from the elements in the regolith below LP and the net

R. C. Elphic, D. J. Lawrence, W. C. Feldman, B. L. Barraclough, Space and Atmospheric Sciences, MS D466, Los Alamos National Laboratory, Los Alamos, NM 87545, USA. S. Maurice, Observatoire Midi-Pyrénées, 31400 Toulouse, France. A. B. Binder, Lunar Research Institute, Gilroy, CA 95020, USA. P. G. Lucey, Hawai'i Institute of Geophysics and Planetology, University of Hawai'i, Honolulu, HI 96822, USA.

*To whom correspondence should be addressed. E-mail: relphic@lanl.gov